Atrophy and hypometabolism patterns in Niemann-Pick type C: A cross-sectional and longitudinal study

Jesús Silva-Rodríguez
University Hospital and Health Research Institute of Santiago de Compostela
Cristina Castro
University Hospital and Health Research Institute of Santiago de Compostela
Julia Cortés
University Hospital and Health Research Institute of Santiago de Compostela
Manuel Arias
University Hospital of Santiago de Compostela
Virginia Pubul
University Hospital and Health Research Institute of Santiago de Compostela
Alexis Moscoso
University of Gothenburg
Idoia Rouco
BioCruces Health Research Institute, Cruces University Hospital
Jordi Gascón
Hospital Universitari de Bellvitge, L'Hospitalet de Llobregat
María Jesús Sobrido
University Hospital of A Coruña
Pablo Aguiar (pablo.aguiar@usc.es)
University Hospital and Health Research Institute of Santiago de Compostela

Article

Keywords: PET, NP-C, MRI, [18F]FDG, Neurology

Posted Date: July 25th, 2022

DOI: https://doi.org/10.21203/rs.3.rs-1847128/v1

Abstract

Purpose

We present a cross-sectional study comparing hypometabolism and atrophy patterns in Niemann–Pick disease type C (NP-C). We also present a longitudinal analysis of NP-C [^{18}F]FDG-PET data.

Methods

22 patients NP-C patients underwent MRI and [^{18}F]FDG-PET imaging at baseline, and a subset of 12 patients were able to complete at least one follow-up PET imaging acquisition. Visual assessment and group-level voxel- and region-based analyses of the baseline MRI and PET images were performed by comparing our NP-C cohort to PET and MRI healthy volunteer cohorts. Per cent changes in metabolism (%/year/region) were calculated for longitudinal analysis.

Results

Significant atrophy was present in the cerebellum ($p < 0.0001$), thalamus ($p < 0.001$), and frontal and hippocampal regions ($p < 0.01$). The most common hypometabolism pattern included severe cerebellum, thalamus and cingulate hypometabolism ($p < 0.0001$), together with mild involvement of cortical areas. [^{18}F]FDG PET provided stronger effect sizes and was able to show significant hypometabolism even in areas without atrophy. [^{18}F]FDG uptake annual changes ($p < 0.01$) were found mainly in the cerebellum (-11%/year) and different frontal and temporal cortical regions (<-2%/year).

Conclusions

Our results add evidence to support the addition of [^{18}F]FDG PET as a tool for the assessment of cross-sectional and longitudinal neurodegeneration in NP-C.

Introduction

Niemann–Pick disease type C (NP-C) is a lysosomal lipid storage disorder with progressive neurological impairment caused by mutations in NPC1 (95% of patients) or NPC2 (5% of patients) genes [1,2]. NP-C exhibits highly variable motor, neuropsychiatric, and neuropsychologic symptoms, including cerebellar ataxia, vertical supranuclear gaze palsy, pyramidal features, dystonia, dysarthria, dysphagia, seizures, progressive hearing loss, major depression, psychosis and cognitive decline [3,4]. Like many rare disorders, diagnosis of NP-C is often challenging and can be time-consuming. The current diagnostic workup includes blood biomarkers (chitotriosidase, oxysterols, bile acids, Lyso-SM-509), NPC1/NPC2 gene sequencing, and filipin staining of unesterified cholesterol in cultured fibroblasts obtained from a skin

biopsy [4]. Since each of these approaches has limitations and pitfalls, and not all of them are available at every clinical setting, different combinations thereof are often applied that may involve screening and confirmatory testing [5].

Nowadays, it is well known that the abnormal neuronal storage of lipids precedes neuronal degeneration in NP-C. This was first described in animal models showing that Purkinje cells in the cerebellum, basal ganglia and thalamus are firstly affected, followed by those in hippocampal and cortical regions [6,7]. These findings were later confirmed in humans using brain magnetic resonance imaging (MRI), which revealed atrophy patterns broadly consistent with the animal model neuropathology. NP-C patients demonstrated significant cerebellar grey and white matter volume reductions, which were associated with ataxia [8], and thalamic and hippocampal reductions [9], while some patients showed atrophy in the midbrain [10] and the corpus callosum [11]. Diffusion tensor imaging (DTI) revealed reductions in fractional anisotropy in major white matter tracts [12–15], which is consistent with the hypothesis of disrupted myelination preceding neuronal cell body loss [16]. All these neuroimaging findings were summarized in the current recommendations for the detection and diagnosis of NP-C [17]. However, these guidelines also warn that MRI abnormalities are detected only in the advanced stages of the disease, pointing to the need for additional imaging modalities that can improve early diagnosis.

Positron emission tomography (PET) with glucose analogue [^{18}F]fluorodeoxyglucose ([^{18}F]FDG) is a well-established tool for imaging neurodegeneration, with accumulating evidence suggesting that [^{18}F]FDG PET functional changes precede atrophy as measured by MRI in several neurodegenerative disorders [18–21]. Previous case reports, suggest that NP-C patients may also present severe hypometabolism even in the presence of very subtle or no MRI abnormalities [22–24]. These findings still need confirmation over a large patient cohort. In addition, recent works have evaluated the use of [^{18}F]FDG PET on NP- C [25,26], but showed some discrepancies on the reported results, so additional evidence is still needed to define a consistent pattern of hypometabolism for the disease. Finally, available longitudinal imaging data on NP-C is limited to two studies evaluating the effects of treatment with miglustat, both qualitatively pointing that miglustat could have a protective effect on cerebellar and subcortical structure [27,28], and that PET imaging is able to measure disease progression.

To add to the existing evidence on the use of [^{18}F]FDG PET on NP-C patients, we conducted a cross-sectional [^{18}F]FDG PET and MRI study in a relatively large cohort of NP-C patients to determine whether there is a characteristic hypometabolic pattern related to NP-C and to investigate if, as hypothesized, hypometabolism precedes atrophy in NP-C. We also acquired longitudinal data to investigate if [^{18}F]FDG PET can track disease progression.

Results

Cohort demographics

Twenty-two patients (13 male, 9 female) with genetically confirmed NP-C were recruited across different Neurology Departments in Spain from 2015 to 2018. The mean age at the start of the study was 38 ± 13.7 years. The average age at symptom onset was 23.5 ± 13.1 years (10 childhood-onset (≤ 16), 12 adult-onset). The average time between the clinical onset and the study was 14.5 ± 9.1 years. Individual demographic and neuroimaging characteristics are summarized in Table 1.

Despite MRI and PET were aimed to be acquired in the same day, the MRI study was delayed for several months (8.74 ± 13.41 months) for ten patients due to patient distress or disability to conduct both scans in the same visit, and it could not even be performed in three patients (indicated in Table 1). Twelve of the twenty-two patients (12/22) were able to complete at least one follow-up visit, in which additional PET images were acquired. Seven patients from Hospital Universitari Bellvitge (patients 7 to 13 in Table 1) had older PET images available which were included in the longitudinal analysis after verifying that they were acquired using the same scanner and protocol. The mean follow-up time including these older acquisitions was 38.1 ± 40.6 months.

Baseline group-level analysis

To obtain voxel-wise spatial patterns of atrophy and glucose hypometabolism, MRI volumetry and PET SPM analyses were carried out by comparing NP-C patients against an age-matched subsets of healthy patients (Fig. 1.a). Our MRI analysis revealed significant atrophy in the cerebellum (maximum z-score = 2.8), thalamus (maximum z-score = 2.6), and hippocampus (maximum z-score = 2.2), with mild affectation of cortical regions (maximum z-score = 1.8), especially on the frontal lobe. In contrast to the MRI, the hypometabolism pattern spreads through the entire cerebellum and limbic system, affecting the cerebellum (maximum z-score = 5.1), cingulate cortex (maximum z-score = 4.7). thalamus (maximum z-score = 4.5), caudate (maximum z-score = 2.9) and midbrain (maximum z-score = 2.5), and large frontal and parietal bilateral cortical regions (maximum z-score = 4.0). No asymmetries were found, neither in the atrophy patterns nor in the hypometabolism maps.

Voxel-wise analysis was complemented by region-base analysis (Fig. 1.b), which largely confirm the voxel-based results. Significant reductions in cortical volume compared to healthy subjects were found in the cerebellum ($p < 0.0001$) and thalamus ($p < 0.001$), middle frontal gyrus and hippocampus ($p < 0.01$), while [^{18}F]FDG uptake was significantly decreased in the cerebellum, thalamus, anterior and posterior cingulate cortices, caudate nucleus, straight gyrus, and orbitofrontal gyrus ($p < 0.0001$); middle frontal gyrus and parahippocampus ($p < 0.001$); and hippocampus, anterior temporal lobe, and putamen ($p < 0.01$). No statistically significant correlations were found between regional uptake (or atrophy) and patient's age ($-0.37 < r < 0.33$), years from clinical onset ($-0.31 < r < 0.42$) or any other relevant demographic variable.

Table 1
Demographic and neuroimaging characteristics

Patient ID	Hospital	Sex	Age, (baseline) y	Clinical onset, y	[^{18}F]FDG PET		MRI
					Number of scans	Follow-up, mo	Delay, mo
P0001	Santiago	M	41	28	2	11	0
P0002	Santiago	F	33	3	2	20	0
P0003	Santiago	F	65	6	2	15	0
P0004	Santiago	F	29	14	1	-	-
P0005	Madrid	F	53	-	1	-	0
P0006	Madrid	F	55	-	1	-	0
P0007	Bellvitge	M	17	11	3	43	9
P0008	Bellvitge	F	35	19	1	-	-
P0009	Bellvitge	F	14	0	3	39	8
P0010	Bellvitge	M	28	12	5	71	47
P0011	Bellvitge	M	26	9	5	83	35
P0012	Bellvitge	M	47	13	3	29	26
P0013	Bellvitge	M	58	26	1	-	-
P0014	Santiago	M	50	7	1	-	0
P0015	Bilbao	M	43	1	2	9	2
P0016	Bilbao	F	41	26	2	9	5
P0017	Santiago	M	17	4	2	96	0
P0018	Málaga	F	38	15	1	-	0
P0019	Santiago	M	26	7	2	32	0
P0020	Bellvitge	M	24	12	1	-	12
P0021	Bellvitge	M	44	30	1	-	14
P0022	Bellvitge	M	43	24	1	-	8

Single-subject Analysis

To assess the usefulness of the obtained group-level hypometabolism patterns for individual patient diagnosis, individual patient images were assessed by visual assessment and by single-subject voxel-

wise analyses. According to reports from two experienced nuclear medicine physicians, the visual inspection repeatedly showed moderate to severe thalamus, cingulate and cerebellum affectation, with generally mild frontotemporal hypometabolism (Fig. 2). Parietal, occipital, and basal ganglia uptakes were largely preserved on most patients according to visual assessment. The left-bottom corner of Fig. 2 shows the median visual pattern. While the results of the visual analysis were consistent with our quantitative analysis, we can observe that the cerebellum, thalamus and cingulate hypometabolism were the key diagnostic features, with 17/22 patients presenting the three features, and 21/22 presenting at least two of the three. Additionally, 17/22 patients showed some degree of frontal hypometabolism. Supplementary Fig. 1 shows the individual quantitative patterns, which showed a good correlation with the visual evaluations. The nuclear physicians reported that the correlation between the patient image and the group-level derived hypometabolism pattern was good or very good for 13/22 (59%) and average for 8/22 patients (36%). One patient was reported to not correlate with the derived pattern (NPC-14 in Fig. 2). More details can be found in supplementary Table 1.

Longitudinal changes in glucose metabolism

Figure 3 presents the longitudinal changes in brain metabolism averaged over all NP-C patients, showing per cent variations in uptake per year. The most significant changes were observed in the cerebellum (-10.92%/year, $p = 0.003$), insula (-2.76%/year, $p = 0.005$) and putamen (-2.49%/year, $p = 0.008$). Anterior orbital gyrus, precentral gyrus, anterior temporal lobe and cuneus also showed progression with $p < 0.05$. No region showed significant increases in metabolism nor asymmetrical changes. Most of the patients with longitudinal data showed consistent progression patterns, as can be observed in Supplementary Figs. 2 and 3, which show the results of single-subject longitudinal analysis.

Discussion

In the present work, we present a cross-sectional and longitudinal neuroimaging study in a multicentre cohort of twenty-two NP-C patients. Our baseline group-level analysis confirmed all expected MRI abnormalities summarized in the current recommendations for the detection and diagnosis of NP-C [17], and was consistent with previously described NP-C neuropathology studies [6,7]. Regarding [^{18}F]FDG, the derived hypometabolism pattern spreads through the cerebellum, thalamus, midbrain, basal ganglia, cingulate cortex and large frontal and parietal cortical regions. On the one hand, our study suggests that PET might be more sensitive than MRI, providing higher effect sizes across the affected areas (Fig. 1). On the other hand, they also suggest that PET can detect earlier signs of neurodegeneration in comparison with MRI, as hypometabolism was found in areas without atrophy, even among patients who had MRI scans delayed for several months (see Table 1). The exception was found in the hippocampus, which seemed to be more affected on the MRI. This could be related to previously reported alterations of the amyloid precursor protein (APP) pathways in NP-C [29], as the behaviour is similar to that of hippocampal atrophy and hypometabolism in Alzheimer's Disease (AD) [30], and deserves to be further studied.

We also provide additional evidence to support the definition of a hypometabolic pattern associated with NP-C, solving some discrepancies between previous works [22–26]. While Lau et al. [25] reported that hypometabolism of the frontal cortex, thalamus and parietal cortex were the most common features in NP-C, Bremova-Ertl et al. [26] reported a different pattern including hypometabolism in the cerebellum, cingulate, parieto-occipital and temporal cortex, but not on the frontal cortex. Our study complements these studies and helps to clarify some discrepancies between them. In our quantitative and visual analysis, cerebellar, thalamic, and cingulate hypometabolism were identified as the most distinctive features, usually combined with heterogeneous cortical (mainly frontal) hypometabolism, as shown in Fig. 2 and Supplementary Fig. 1. Improvements might be related with the more sophisticated quantification methods in use and larger sample size. Cerebellar, thalamic, and cingular signatures were present in 17/22 patients, and at least two of the three were present in 21/22 patients. Frontal hypometabolism was found in 17/22 patients. A combination of frontal and thalamic hypometabolism has been reported in frontotemporal dementia disorders [31,32], while posterior cingulate hypometabolism has been described as a common early sign of AD and dementia with Lewy bodies [33,34]. Cerebellar hypometabolism has been reported in several spinocerebellar ataxias [35]. Nevertheless, the reported combination of hypometabolic features (cerebellum, thalamus and cingulate) combined with frontal hypometabolism, might be unique to NP-C, supporting the inclusion of [^{18}F]FDG PET in the NP-C diagnostic work-up. More meaningful, this combination of features is in good agreement with previous knowledge in NP-C disease progression [6,7].

We also performed [^{18}F]FDG PET longitudinal analysis on a subsample of patients, in which we were able to measure significant annual decreases of glucose metabolism in the cerebellum (annual decrease 11%, $p < 0.005$) and less pronouncedly in the insula, thalamus, putamen, precentral gyrus, and anterior orbital gyrus (annual decrease > 2%, $p < 0.01$). To date, longitudinal [^{18}F]FDG PET in NP-C patients was available only in a cohort of sixteen paediatric patients, showing that brain hypometabolism can be stabilized in children under treatment with miglustat [27]. In adult-onset NP-C patients, only an MRI-based study was carried out to assess treatment effects of miglustat on cerebellar and subcortical volumes, showing evidence that miglustat could have a protective effect on cerebellar and subcortical structure [28]. Our results show that [^{18}F]FDG PET can measure disease progression on NP-C, and postulates the annual change in cerebellum metabolism as a candidate biomarker for assessing disease progression and treatment response in NP-C. Individual progression (shown in Supplementary Figs. 2 and 3) shows that individual patients presented consistent longitudinal progression patterns in [^{18}F]FDG PET.

The current study also presents some limitations. The first one is the number of patients. Regarding this, it is important to consider that NP-C is a rare and highly disabling disease, and this is, to the best of our knowledge, still the largest study including PET on an NP-C cohort, and the only one including concurrent PET and MRI. MRI imaging was delayed several months for some of the participants due to patient disabilities to perform both scans on the same day. Finally, patients were included in the study indistinctively of being under therapy, which might have biased our longitudinal analysis by reducing the

effect size. In addition, longitudinal MRI was not available, so a comparison between longitudinal PET and MRI could not be performed.

Taken together, our cross-sectional and longitudinal results lead to the definition (refinement) of a distinctive hypometabolism pattern of NP-C that has not been observed in other neurodegenerative conditions, and shows that [^{18}F]FDG PET might be a more suitable imaging modality than MRI for the diagnosis of NP-C. Due to these findings, we strongly believe that [^{18}F]FDG PET may constitute a useful clinical tool to support the differential diagnosis of NP-C. Furthermore, as the progression in cerebellar hypometabolism is associated with clinical deterioration, cerebellar glucose metabolism may also constitute an imaging biomarker to assess the progression and possible treatment responses in NP-C.

Methods

Patient Recruitment and Clinical Evaluation

This is a national, multicenter observational study. The protocol for the study was approved by the Galician Research Ethics Committee, and all the experiments were performed in accordance with the Declaration of Helsinki and related policies in Spain and Europe. The aims and study protocol were disseminated through various Spanish scientific networks for rare diseases, metabolic diseases and movement disorders, and patient associations to recruit patients fulfilling recruitment criteria and willing to participate. Eligible subjects must have a genetically confirmed diagnosis of NP-C (any combination of clinical manifestations and ongoing treatments was permitted). Subjects with an uncertain diagnosis, medical contraindication for [^{18}F]FDG PET, severe disability due to NP-C or other concomitant diseases (Barthel Index for Activities of Daily Living (ADL) $\leq$ 20) or unable to reach to nearest reference Hospital, were excluded. Informed consent was obtained from all participants and/or their legal guardians.

Retrospective data collection was completed by the patient´s referring physician and the clinical collaborators of the study, including demographic and clinical data (gender, age at the moment of data collection, age at the beginning of the disease, age at diagnosis, first symptoms, years of evolution, time of treatment, family history, observational prospective neurological evaluation, subjective evaluation, pertinent complementary tests) and diagnostic tests (genetic test, filipin staining, biochemical analysis, ultrasounds, electroencephalography, videonystagmography and disability score).

Neuroimaging studies

Participants travelled to the city of the nearest reference hospital the day before neuroimaging acquisition to facilitate having similar basal conditions (avoiding same day travelling from distant locations, too early wake-up, etc…). MRI and PET scans were acquired in the same morning after at least 8 hours of fasting. After baseline acquisitions, patients were re-scheduled for yearly follow-up visits during the length of the study. In the follow-up visits, only PET imaging was performed. MRI and PET acquisition protocols were as follows:

- Structural MRI studies: The used MR scanners were: Philips Achieva (Hospital Clínico de Santiago de Compostela and Centro de Investigaciones Médico-Sanitarias, Málaga), Siemens Biograph mMR (Hospital Puerta de Hierro, Madrid), Siemens Magnetom Vida (Clínica Corachan, Barcelona) and Siemens Magnetom Essenza (Hospital de Cruces, Bilbao). All the acquisitions were performed with the same protocol, including T1-weighted 3D TFE axial high-resolution images, with TR, 8.73 milliseconds; TE, 3.96 milliseconds; section thickness, 0.8 mm; and distance, 0.4 mm.
- [^{18}F]FDG PET studies: after the intravenous injection of 370MBq of [^{18}F]FDG, patients were asked to lay at rest in a dark and quiet room. Starting 45 minutes after injection, they were scanned over 30 minutes using a single-bed acquisition including the whole brain (special care was taken to include the whole cerebellum). The PET scanners in use were: GE Advance NXi (Hospital Clínico de Santiago de Compostela), Siemens Biograph mMR (Hospital Puerta de Hierro, Madrid), GE Discovery ST (Hospital Universitari Bellvitge, Barcelona and Centro de Investigaciones Médico Sanitarias, Málaga) and GE Discovery 690 (Hospital Cruces, Bilbao). All the acquisitions were performed using the default scanner protocols and reconstruction was performed using the iterative algorithm provided by each manufacturer using the recommended settings for brain imaging.

Harmonization and image analysis

To take into account possible differences between the scanners, the analysis of the multicenter MRI and [^{18}F]FDG PET images was performed using the Neurocloud® platform from Qubiotech (https://www.qubiotech.com/en/solutions/), which provides validated harmonization pipelines for the different MRI and PET scanners. The software provides a simple, automatic and easy-to-use interface to most SPM12 functionalities and several of its toolboxes [36], incorporates a CE-mark and meets the requirements for its use as a diagnostic tool in all European countries. The analyses pipelines were the following:

MRI and PET harmonization and processing

MRI harmonization began with a spatial adaptive non-local means denoising filter [37], followed by an internal resampling to deal with low-resolution images and anisotropic spatial resolution. The data were then bias-corrected and affine-registered, followed by the standard SPM “unified segmentation” [38]. The output of the segmentation was used for skull-stripping and the brain was then parcellated into left and right hemispheres, subcortical areas, and cerebellum. Subsequently, a local intensity transformation of all tissue classes was performed to reduce the effects of higher grey matter intensities in the motor cortex, basal ganglia, or occipital lobe before the final adaptive maximum a posteriori (AMAP) segmentation. This final AMAP segmentation step [39] was refined by applying a partial volume estimation [40]. Finally, the tissue segments were spatially normalized to the Montreal Neurological Institute (MNI) reference space using DARTEL [41].

To harmonize PET images from different PET scanners with different spatial resolutions, specific smoothing kernels for each scanner were applied to achieve an isotropic resolution of 8 mm FWHM. Next,

PET harmonization included a standard twelve-parameter affine spatial normalization as implemented in SPM12 [36] using an [^{18}F]FDG template derived from a healthy subject database previously acquired at our centre [42] and incorporated into Neurocloud®. The database incorporates 78 healthy volunteers with ages between 20 and 88 (average age is 58) previously acquired using the aforementioned [^{18}F]FDG PET acquisition protocol for the GE Advance NXi. Finally, a data-driven histogram-based intensity normalization method was applied for performing global glucose metabolism scaling while preserving the metabolism of healthy areas [43]. In brief, the histogram-based intensity normalization works as follows: each PET image is smoothed and voxel-wise divided by the [^{18}F]FDG template (including only voxels inside a parenchyma mask). The result is a map of scaling factors by voxel. These values are histogrammed and the most prevalent scaling factor (maximum of the histogram) is considered the correct normalization factor. This method seeks to perform scaling in the healthy areas while avoiding pathological areas and has demonstrated to be reliable in the presence of large hypometabolism (which we expected to find in NPC) where other normalization methods tend to fail [43].

MRI analysis

MRI volumetry was carried out by comparing NP-C patients against an age-matched subset of 100 subjects from a 600 subject database which was previously derived by combining healthy volunteers from the IXI (brain-development.org) and OASIS (oasis-brains.org) databases. Healthy subjects underwent the same harmonization process used for our NP-C patients. Two image analysis techniques were used:

- **Voxel-based morphometry (VBM)**: grey matter VBM analysis was conducted as implemented in CAT12 [38]. Age at MRI acquisition and gender were used as confounding nuisance covariates. Statistical differences between NP-C patients and controls were transformed to z-scores and overlapped to a brain template (ICBM152) after applying a threshold of z-score = 1.5 and a minimum cluster size of 250 voxels. Only reductions in volume were considered, while volume increases were only visually inspected to identify any potential artefacts.
- **Region-based morphometry**: Region-based analysis was performed as implemented in CAT12, using predefined volumes of interest (VOIs) from the Hammersmith atlas [44]. Comparisons between the NP-C group and the age-matched healthy group were performed for each region by using two-sample t-tests (p-values < 0.01 were considered significant). Statistical differences were overlapped to a rendered brain template (CH2).

PET analysis

Quantitative PET analysis was performed using the same two strategies, comparing NP-C patients to the aforementioned control database of 78 control subjects:

- **Voxel-based analysis**: we conducted a voxel-wise analysis using the conventional two-sample t-test statistical comparisons in SPM12 [36], resulting in a parametric image showing voxel-by-voxel differences between NP-C patients and controls. Age at PET acquisition and sex were used as

confounding nuisance covariates. As previously, statistical differences (transformed to z-scores) between NP-C and controls were overlapped to an ICBM152 brain template after applying a threshold of z-score = 1.5 and a minimum cluster size of 250 voxels. Only hypometabolism was considered, while hypermetabolism was only visually inspected to verify a correct intensity scaling.

- **Region-based analysis**: the VOIs included in the Hammersmith atlas were overlapped to the patient and healthy subject's [^{18}F]FDG PET images in NMI space and the average [^{18}F]FDG uptake (in arbitrary units after intensity normalization) for each VOI was calculated. Group comparisons were performed for each VOI using two-sample t-tests (p-values < 0.01 were considered significant).

Single-subject analysis

To assess the usefulness of the obtained hypometabolism patterns derived at the group-level analysis for individual patient diagnosis, we performed two additional evaluations. First, we conducted additional single-subject voxel-wise analyses comparing each NP-C subject with the healthy database. For this, we applied the single-subject analysis pipelines incorporated in Neurocloud®, which apply a statistical non-parametric mapping approach (SnPM, http://www.nisox.org/Software/SnPM13/). Second, we performed a visual assessment and rating of each patient's [^{18}F]FDG PET image. Two experienced nuclear medicine physicians assigned a consensus score of 0 (none), 1 (mild), 2 (moderate), or 3 (severe) hypometabolism to frontal, temporal, parietal, occipital and cingulate cortical regions, thalamus, basal ganglia, and cerebellum, based on plain visual assessment. Physicians were also asked to score between 0 (none), 1 (average), 2 (good) and 3 (very good) the agreement between the visual presentation and the derived group-level hypometabolism pattern.

Longitudinal analysis

For longitudinal analysis, individual per cent changes in metabolism (%/year/region) were calculated based on the region-based analysis (using the deviation from the average healthy subject's metabolism as a metric). The significance of the calculated changes was assessed by using paired t-tests.

Declarations

Declarations

Competing Interests

This study was funded by Actelion Pharmaceuticals Ltd, makers of Zavesca (miglustat), a common NP-C treatment. JSR and PA are consultants for Qubiotech Health Intelligence SL (www.qubiotech.com), makers of Neurocloud, the image analysis software used in this study. Other authors do not have any Competing Interests. No other potential conflicts of interest relevant to this article exist.

Author Contributions

PA, JG and MJS contributed to the design of the study. CC was the clinical and recruitment manager. MA, IR, and JG contributed to the patient recruitment. JSR and AM performed the data processing and analysis. JSR drafted the original manuscript. JC and VP performed the individual visual analysis. PAF and MJS contributed to the critical revision of the manuscript. All authors discussed the results and implications and commented on the manuscript. All authors read and approved the final manuscript.

Acknowledgements

The authors want to thank all the scientific societies and patient associations who made this work possible. Also, the patients that while dealing with great disabilities decided to contribute to this study. This work was supported by EAPA_791/2018 (NeuroAtlantic Project, JSR) and RYC-2015/17430 (Ramón y Cajal, PA).

References

1. Vanier, M. T. & Millat, G. Niemann-Pick disease type C. *Clin. Genet.* **64**, 269–281 (2003).
2. Sleat, D. E. *et al.* Genetic evidence for nonredundant functional cooperativity between NPC1 and NPC2 in lipid transport. *Proc. Natl. Acad. Sci. U. S. A.* **101**, 5886–5891 (2004).
3. Iturriaga, C., Pineda, M., Fernández-Valero, E. M., Vanier, M. T. & Coll, M. J. Niemann-Pick C disease in Spain: clinical spectrum and development of a disability scale. *J. Neurol. Sci.* **249**, 1–6 (2006).
4. NP-C Guidelines Working Group *et al.* Recommendations on the diagnosis and management of Niemann-Pick disease type C. *Mol. Genet. Metab.* **98**, 152–165 (2009).
5. Sobrido, M.-J. *et al.* Recommendations for patient screening in ultra-rare inherited metabolic diseases: what have we learned from Niemann-Pick disease type C? *Orphanet J. Rare Dis.* **14**, 20 (2019).
6. Brown, D. E. *et al.* Feline Niemann-Pick disease type C. *Am. J. Pathol.* **144**, 1412–1415 (1994).
7. Ong, W. Y. *et al.* Neurodegeneration in Niemann-Pick type C disease mice. *Exp. Brain Res.* **141**, 218–231 (2001).
8. Walterfang, M. *et al.* Cerebellar volume correlates with saccadic gain and ataxia in adult Niemann-Pick type C. *Mol. Genet. Metab.* **108**, 85–89 (2013).
9. Walterfang, M. *et al.* Subcortical volumetric reductions in adult Niemann-Pick disease type C: a cross-sectional study. *AJNR Am. J. Neuroradiol.* **34**, 1334–1340 (2013).
10. Walterfang, M. *et al.* Pontine-to-midbrain ratio indexes ocular-motor function and illness stage in adult Niemann-Pick disease type C. *Eur. J. Neurol.* **19**, 462–467 (2012).
11. Walterfang, M. *et al.* Size and shape of the corpus callosum in adult Niemann-Pick type C reflects state and trait illness variables. *AJNR Am. J. Neuroradiol.* **32**, 1340–1346 (2011).
12. Walterfang, M. *et al.* White and gray matter alterations in adults with Niemann-Pick disease type C: a cross-sectional study. *Neurology* **75**, 49–56 (2010).

13. Masingue, M. *et al.* Evolution of structural neuroimaging biomarkers in a series of adult patients with Niemann-Pick type C under treatment. *Orphanet J. Rare Dis.* **12**, (2017).
14. Trouard, T. P., Heidenreich, R. A., Seeger, J. F. & Erickson, R. P. Diffusion tensor imaging in Niemann-Pick Type C disease. *Pediatr. Neurol.* **33**, 325–330 (2005).
15. Scheel, M., Abegg, M., Lanyon, L. J., Mattman, A. & Barton, J. J. Eye movement and diffusion tensor imaging analysis of treatment effects in a Niemann-Pick Type C patient. *Mol. Genet. Metab.* **99**, 291–295 (2010).
16. You, Y. *et al.* Demyelination precedes axonal loss in the transneuronal spread of human neurodegenerative disease. *Brain* **142**, 426–442 (2019).
17. Patterson, M. C. *et al.* Recommendations for the diagnosis and management of Niemann-Pick disease type C: an update. *Mol. Genet. Metab.* **106**, 330–344 (2012).
18. Mosconi, L. *et al.* Hypometabolism exceeds atrophy in presymptomatic early-onset familial Alzheimer's disease. *J. Nucl. Med. Off. Publ. Soc. Nucl. Med.* **47**, 1778–1786 (2006).
19. Gordon, B. A. *et al.* Spatial patterns of neuroimaging biomarker change in individuals from families with autosomal dominant Alzheimer's disease: a longitudinal study. *Lancet Neurol.* **17**, 241–250 (2018).
20. Tang, C. C. *et al.* Metabolic network as a progression biomarker of premanifest Huntington's disease. *J. Clin. Invest.* **123**, 4076–4088 (2013).
21. Albrecht, F., Ballarini, T., Neumann, J. & Schroeter, M. L. FDG-PET hypometabolism is more sensitive than MRI atrophy in Parkinson's disease: A whole-brain multimodal imaging meta-analysis. *NeuroImage Clin.* **21**, 101594 (2019).
22. Kumar, A. & Chugani, H. T. Niemann-Pick disease type C: unique 2-deoxy-2[^{18}F] fluoro-D-glucose PET abnormality. *Pediatr. Neurol.* **44**, 57–60 (2011).
23. Huang, J.-Y. *et al.* Neuroimaging findings in a brain with Niemann-Pick type C disease. *J. Formos. Med. Assoc. Taiwan Yi Zhi* **110**, 537–542 (2011).
24. Benussi, A. *et al.* Phenotypic heterogeneity of Niemann-Pick disease type C in monozygotic twins. *J. Neurol.* **262**, 642–647 (2015).
25. Lau, T. Y. *et al.* Brain hypometabolic changes in 14 adolescent–adult patients with Niemann–Pick disease type C assessed by 18F-fluorodeoxyglucose positron emission tomography. *J. Neurol.* (2021) doi:10.1007/s00415-021-10535-4.
26. Bremova-Ertl, T. *et al.* Clinical, ocular motor, and imaging profile of Niemann-Pick type C heterozygosity. *Neurology* **94**, e1702–e1715 (2020).
27. Pineda, M. *et al.* Clinical experience with miglustat therapy in pediatric patients with Niemann-Pick disease type C: a case series. *Mol. Genet. Metab.* **99**, 358–366 (2010).
28. Bowman, E. A. *et al.* Longitudinal changes in cerebellar and subcortical volumes in adult-onset Niemann-Pick disease type C patients treated with miglustat. *J. Neurol.* **262**, 2106–2114 (2015).

29. Mattsson, N. *et al.* Amyloid-β metabolism in Niemann-Pick C disease models and patients. *Metab. Brain Dis.* **27**, 573–585 (2012).
30. Chetelat, G. *et al.* Direct voxel-based comparison between grey matter hypometabolism and atrophy in Alzheimer's disease. *Brain* **131**, 60–71 (2007).
31. Diehl-Schmid, J. *et al.* FDG-PET underscores the key role of the thalamus in frontotemporal lobar degeneration caused by C9ORF72 mutations. *Transl. Psychiatry* **9**, 54 (2019).
32. Jeong, Y. *et al.* 18F-FDG PET findings in frontotemporal dementia: an SPM analysis of 29 patients. *J. Nucl. Med. Off. Publ. Soc. Nucl. Med.* **46**, 233–239 (2005).
33. Kato, T., Inui, Y., Nakamura, A. & Ito, K. Brain fluorodeoxyglucose (FDG) PET in dementia. *Ageing Res. Rev.* **30**, 73–84 (2016).
34. Whitwell, J. L. *et al.* 18F-FDG PET in Posterior Cortical Atrophy and Dementia with Lewy Bodies. *J. Nucl. Med. Off. Publ. Soc. Nucl. Med.* **58**, 632–638 (2017).
35. Aguiar, P. *et al.* PET and MRI detection of early and progressive neurodegeneration in spinocerebellar ataxia type 36: Pet And Mri Patterns Of Sca36. *Mov. Disord.* **32**, 264–273 (2017).
36. Ashburner, J. SPM: a history. *NeuroImage* **62**, 791–800 (2012).
37. Manjón, J. V., Coupé, P., Martí-Bonmatí, L., Collins, D. L. & Robles, M. Adaptive non-local means denoising of MR images with spatially varying noise levels. *J. Magn. Reson. Imaging JMRI* **31**, 192–203 (2010).
38. Ashburner, J. & Friston, K. J. Unified segmentation. *NeuroImage* **26**, 839–851 (2005).
39. Rajapakse, J. C., Giedd, J. N. & Rapoport, J. L. Statistical approach to segmentation of single-channel cerebral MR images. *IEEE Trans. Med. Imaging* **16**, 176–186 (1997).
40. Tohka, J., Zijdenbos, A. & Evans, A. Fast and robust parameter estimation for statistical partial volume models in brain MRI. *NeuroImage* **23**, 84–97 (2004).
41. Ashburner, J. A fast diffeomorphic image registration algorithm. *NeuroImage* **38**, 95–113 (2007).
42. Aguiar, P. *et al.* PET and MRI detection of early and progressive neurodegeneration in spinocerebellar ataxia type 36. *Mov. Disord. Off. J. Mov. Disord. Soc.* **32**, 264–273 (2017).
43. López-González, F. J. *et al.* Intensity normalization methods in brain FDG-PET quantification. *NeuroImage* **222**, 117229 (2020).
44. Hammers, A. *et al.* Three-dimensional maximum probability atlas of the human brain, with particular reference to the temporal lobe. *Hum. Brain Mapp.* **19**, 224–247 (2003).

Figures

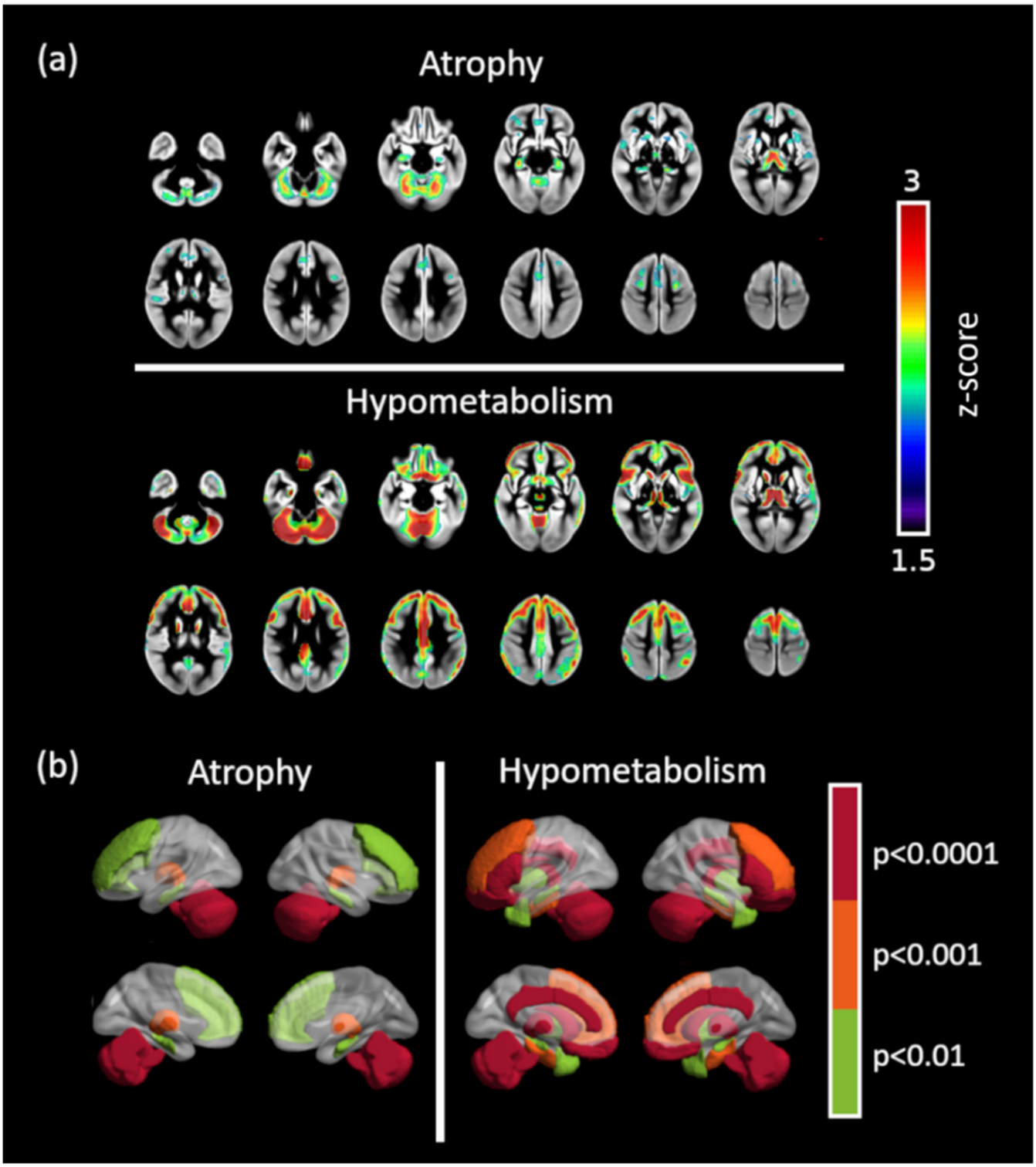

Figure 1

Average patterns of atrophy and hypometabolism. a) Voxel-wise analysis. b) Region-based analysis

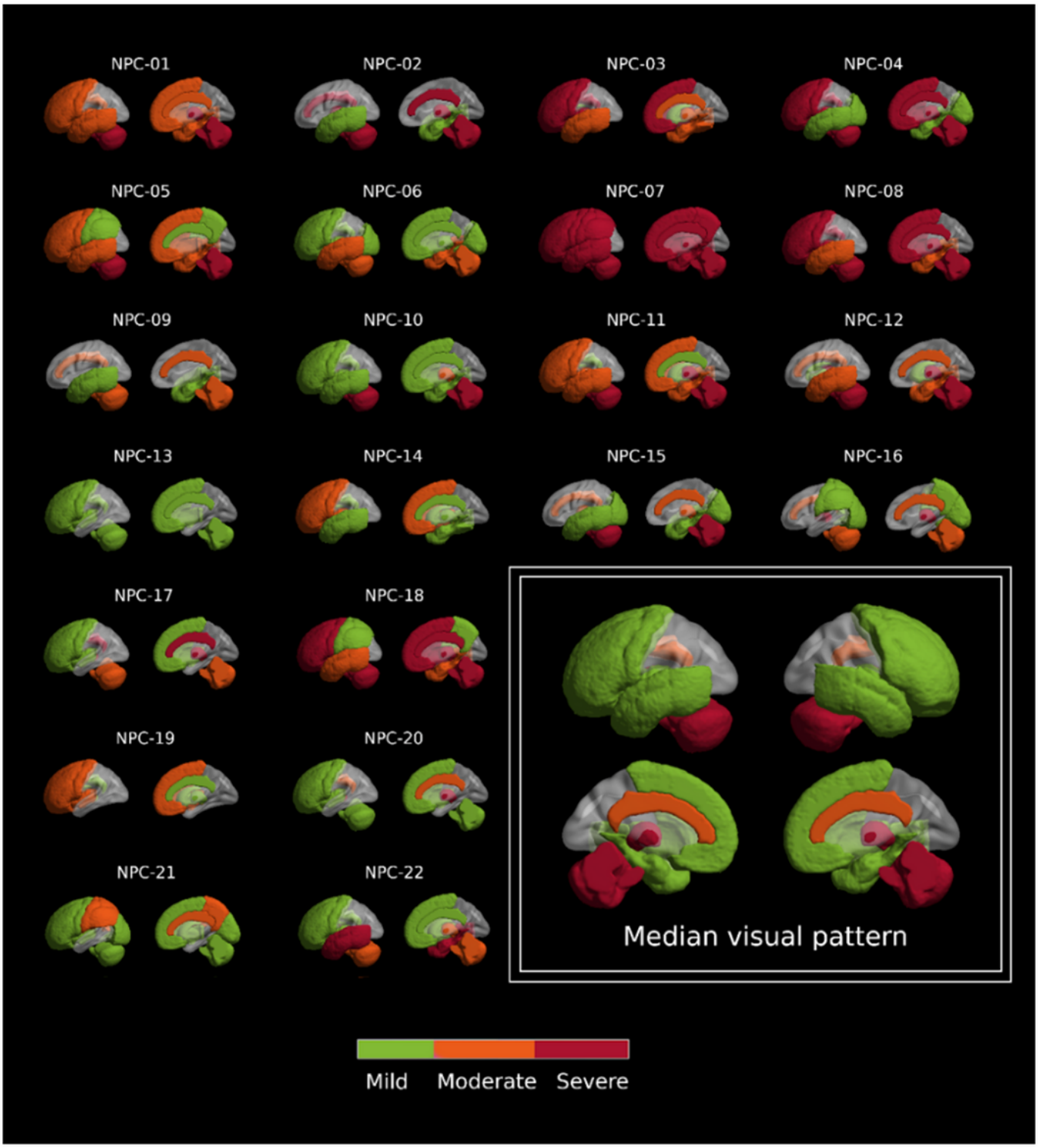

Figure 2

Visual patterns for each of the 22 NP-C patients. In the right-bottom, the median visual pattern across the whole database.

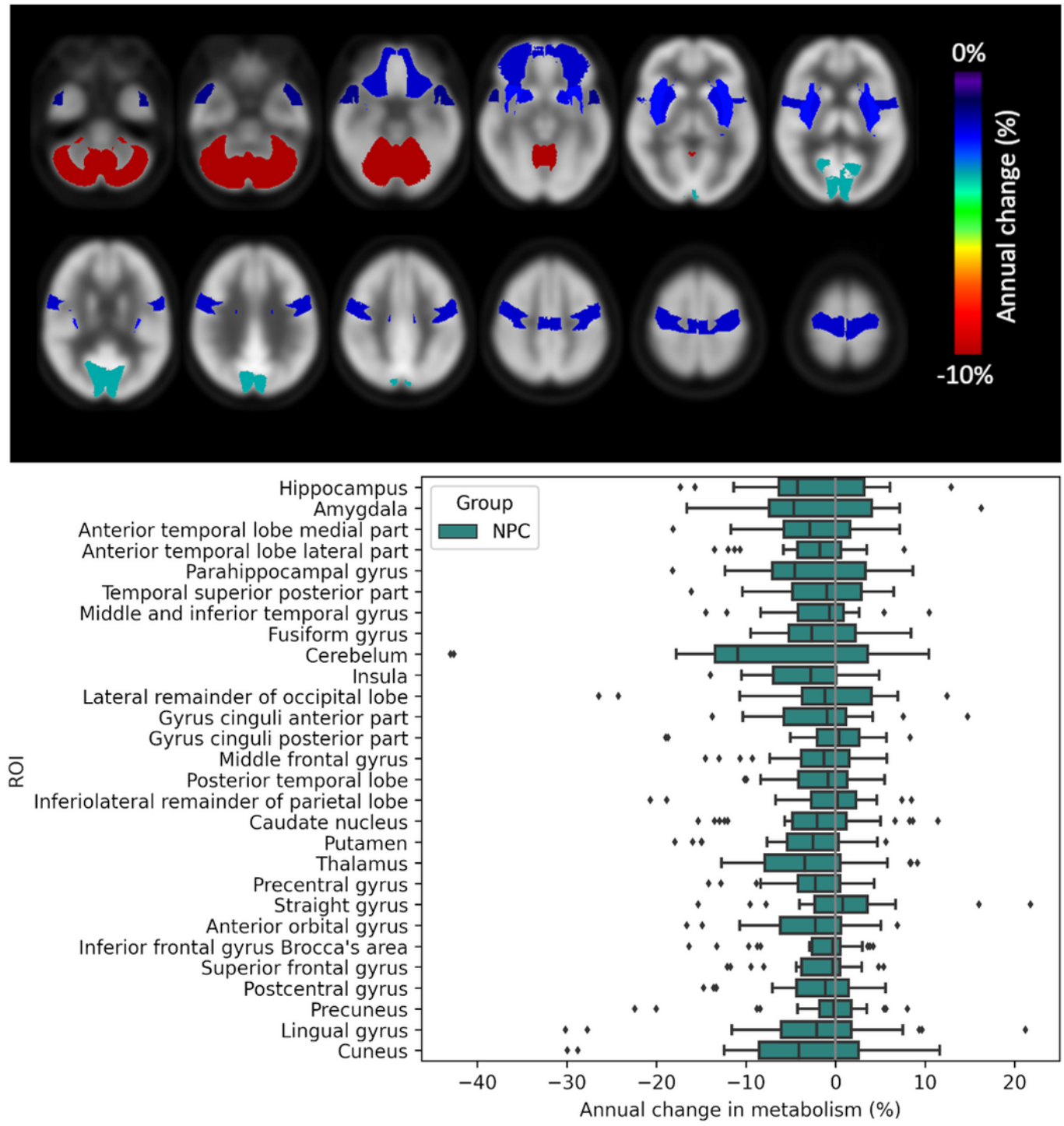

Figure 3

Average annual change in glucose metabolism across the Hammersmith atlas ROIs.

Supplementary Files

This is a list of supplementary files associated with this preprint. Click to download.

- SupplementaryMaterial.docx